JOURNAL OF SPACECRAFT AND ROCKETS
Vol. 42, No. 1, January–February 2005

Aerodynamics of Low-Blowing-Ratio Fuselage Injection into a Supersonic Freestream

Zakaria Mahmud* and Rodney D. W. Bowersox†
Texas A&M University, College Station, Texas 77843

A parametric characterization of the surface flow structure and associated aerodynamic loading for injection into a Mach 3.0 freestream through jets mounted into the side of missile fuselage (sharp-coned cylinder) was experimentally achieved. The experimental methods included surface oil flow visualization, shadowgraph photography, and pressure-sensitive paint. The range of jet-to-freestream pressure ratios spanned 0.6–19.0, which corresponds to an effective backpressure ratio range of 0.19–6.15. Hence, overexpanded, perfectly expanded, and underexpanded jets were tested. The temperature ratios spanned 1.0–13.6, where helium was used to simulate the highest temperature. The nondimensional momentum parameter ratio (MPR) varied over a range of 0.005–0.09. It was observed that the injection temperature for a given MPR had a small effect on the boundary-layer separation distance. For the range of conditions tested, the interaction force increased linearly with increasing MPR. The amplification factors for the lowest MPR values were found to be higher than expected trends.

Nomenclature

A_b	=	missile blockage area
A_e	=	jet exit area
A_F	=	missile fuselage area
C_F	=	total jet thrust coefficient, $F/(\frac{1}{2}\rho_\infty u_\infty^2 A_b)$
D	=	diameter
F	=	net force, $F_j + F_s$
F_j	=	jet momentum force
F_s	=	surface interaction force
I	=	pressure-sensitive paint image intensity
I_{ref}	=	Reference pressure-sensitive paint image intensity
K_F	=	force amplification factor
M	=	Mach number
$\dot{m}_j$	=	jet mass flow rate
P	=	pressure
$\bar{P}_e$	=	average pressure around the periphery of the jet exit
P_{eb}	=	effective backpressure
$\bar{P}_F$	=	average fuselage pressure
$P_{F,\infty}$	=	freestream pressure above the missile fuselage
P_t	=	stagnation pressure
T	=	temperature
T_t	=	stagnation temperature
u	=	axial velocity
v	=	transverse velocity
x, y, z	=	Cartesian coordinates
Δ	=	jet upstream separation distance
γ	=	ratio of specific heats
ρ	=	density

Subscripts

j	=	jet exit condition
∞	=	freestream

Received 26 August 2003; revision received 23 January 2004; accepted for publication 29 January 2004.

*Postdoctoral Research Associate, Aerospace Engineering Department. Member AIAA.

†Associate Professor, Aerospace Engineering Department. Associate Fellow AIAA.

Introduction

JETS have the potential to be an effective means of controlling aerodynamic characteristics of high-speed vehicles and weapon systems. One application is the use of reaction control jets for rapid maneuvering of high-speed intercept missiles. Hypersonic interceptor designs typically include several lateral jets used for divert and/or altitude control. Air-to-air interceptors usually require a continuous and long-duration reaction control jet for accuracy and rapid maneuverability. In addition, confined space firing (e.g., antitank or guerrilla warfare) missile control systems are required to be effective at low speed with good maneuverability and very short response time.[1]

The flowfield structure of a jet issuing from a curved body of revolution is qualitatively similar to that over a flat surface.[2] The quantitative information varies due to the three-dimensional effect of the curved surface.[3–10] Based on the available data,[2–10] the overall three-dimensional structure of a jet emerging from an axisymmetric body is sketched (Fig. 1). There appears to be at least four vortical flow motions created by the transverse jet in a crossflow.[7] As the jet emerges into the crossflow, it is curved downstream by the crossflow. The jet plume acts as a cylindrical obstacle to the crossflow and creates an adverse pressure gradient, which eventually generates a wraparound horseshoe vortex on the surface. Then the jet plume evolves into the "kidney bean" shape, which is due to the counter-rotating vortex pair. This counter-rotating vortex pair dominates the downstream flow.[8] The origin of this vortex pair is predicted to be near the jet exit and caused by the lateral shearing along the plume edges and the pressure gradient due to turning the injectant flow into the freestream direction. A ringlike vortex structure appears in the wake region. These alternating vertical vortices, sometimes called the wake vortices, give the appearance of a "Karman vortex street."[9] The wake vortices were believed to originate from the crossflow boundary layer and to end in the jet plume. The horseshoe vortices and the counter-rotating vortices are mean flow characteristics of the jets in a crossflow, whereas the shear-layer vortices and the wake vortices are intrinsically unsteady.

Accurate aerodynamic characterization of the jet interaction with the missile body is essential for the design of an autopilot. One important parameter of jet interaction is the amplification factor, which is defined as the ratio of the effective force to the vacuum thrust. Vacuum thrust is the net reaction force created when a jet is fired in a vacuum; this force is equivalent to the thrust of a rocket engine. However, in a sensible atmosphere, the net force produced between the jet and freestream can be higher or lower than the vacuum thrust. In the extreme case, the net force on an axisymmetric

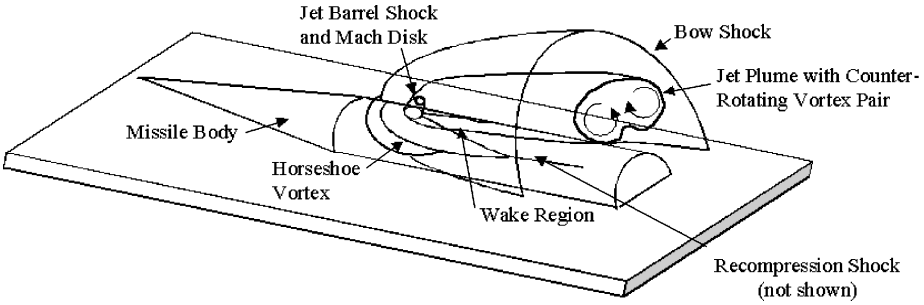

Fig. 1 Flowfield schematic.

body can be the opposite of what is expected, a situation known as control reversal.[11] When a jet is first fired into a supersonic crossflow, a shock wave upstream of the jet is created (Fig. 1). The high pressures associated with the shock cause a positive amplification. A portion of the shock that wraps around the missile fuselage creates a high-pressure region under the axisymmetric body causing a deamplification on the net force. Also, the low-pressure wake region downstream of the jet causes further deamplification. If the total deamplification is higher than the total amplification, the net force will be opposite of what is anticipated. The most severe deamplification happens at low altitudes, low Mach numbers, and low angle of attack.

Roger[12] documented a number of parameters that can affect thruster control effectiveness. A subset of salient parameters are the freestream Mach number M_∞, the jet Mach number M_j, the jet momentum parameter ratio (MPR), the jet pressure ratio P_j/P_∞, the jet temperature ratio T_j/T_∞, the Reynolds number Re, and the jet gas ratio of specific heats, γ_j. In addition to these parameters, jet geometry and chemical reactions within the plume were also identified as important, especially for flow separation.[12]

Of relevance here, flight control of supersonic missiles at low altitudes using low-blowing-ratio reaction jets is complicated due to 1) nonlinear, counterintuitive surface interactions, 2) hot gas effects, and 3) poor predictability using modern computational fluid dynamic codes, where turbulence modeling is a key factor limiting the accuracy.[13] Furthermore, it has been documented[1–8] that jet-interaction experimental data is lacking, and high-quality systematic experimental studies to build a database are needed. The principal objective of the present research is to experimentally characterize the mean plume structure and aerodynamic loading of high-speed jet-interaction flowfields at low-Mach, low-altitude, and low-blowing-ratio operating conditions.

Facilities and Instrumentation

Supersonic Wind Tunnel and Models

The experiments took place in a Mach 3.0 wind tunnel. The measured Mach number was 2.97 ± 0.04 with a variation across the test section. The tunnel operating conditions were $P_t = 0.62 \pm 0.1$ MPa, $T_t = 285 \pm 2.2$ K. The freestream turbulence was nominally 3.0%, and the boundary-layer thickness at the nozzle exit was 4.8 mm. The dimensions of the test section were $7.62 \times 7.62 \times 30.5$ cm^3.

The wind-tunnel models were half-body three-dimensional blended-wall missile fuselages (as shown in Fig. 1). The wind-tunnel models were bolted to the floor of the test section as shown in Fig. 2a. A single port circular injector was machined into each model. The models were 19.05 cm long, 3.56 cm in diameter (D), with 13-deg half-cone angles. A schematic of the models can be seen in Fig. 2b. Four models with different injectors were used for the current research. The models were designated M3A-HP (Mach 3, air injectant, high injection pressure), M3A-LP (Mach 3, air injectant, low injection pressure), M3H (Mach 3, helium injectant), and M1A (Mach 1, air injectant). Model M3H was operated with compressed helium gas and the rest were operated with compressed air. Detailed injector dimensions and operating conditions are listed in Table 1.

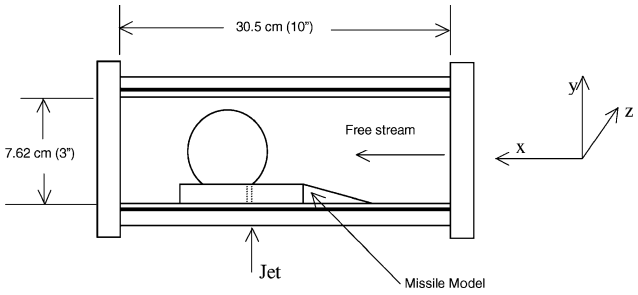

a) Test section

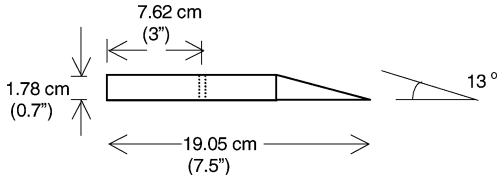

b) Missile model

Fig. 2 Wind-tunnel schematics.

A pebble bed heater was designed and constructed for high-temperature injection. The hot jet injection surface oil flow visualization (SOFV) was performed at 1190°F (916 K). Because of safety concerns, this hot jet interaction flowfield visualization was performed only for the sonic model, which was operated at near atmospheric pressure. Helium was used to simulate higher temperatures because Champigny and Lacau[1] documented that helium at ambient temperatures can be used to simulate air at approximately 2000 K. The available temperature operating conditions are also listed in Table 1.

The flow conditions (summarized in Table 1) were selected to span an important and poorly characterized operating domain for Army missiles,[13] specifically with low-altitude, low-momentum-ratio supersonic flight.

Flow Visualization

Dow Corning 200 fluid (1000 CST) was used for surface oil flow visualization. The oil, mixed with orange fluorescent dye (Day-Glo Color Corp.; pigment sample T-15 blaze orange), was smeared onto the test surface and illuminated by an ultraviolet lamp. A charge-coupled device (CCD) camera (Kodak Professional DCS 460c, resolution 3060×2036 with a Nikon N90 50-mm lens) mounted on top of the test section was used to collect the images of the flow structure during the tunnel run condition.

The shadowgraph setup was relatively simple. A single concave collimating mirror was used to create a collimated light beam that passed through the test section sidewall windows and onto a screen. The Kodak camera system (described earlier) was used to capture the image on the screen. For the schlieren images, the collimated beam that passed through the test section was projected onto a second mirror. The color knife edge was located at the focal point of the reflected beam. The diverging beam was viewed on the screen, and the CCD camera captured the color image.

Table 1 Injector operating conditions and separation distance results

Model	M_j	Gas	D_j, mm	D_j/D_t	P_{tj}, MPa	P_j/P_∞	P_j/P_{eb}	P_j/P_{eb}	T_{tj}, K	T_j/T_∞	A_b/A_e	MPR	Δ/De	C_F	K_F
M3A-HP	3.0	Air	2.45	2.06	5.96	9.38	3.07	3.07	294.0	1.0	210.2	0.05	2.08	0.197	2.18
					12.9	18.8	6.15	6.15				0.09	2.81	0.286	1.57
M3A-LP	3.0	Air	8.18	2.06	0.377	0.60	0.19	0.19	294.0	1.0	18.9	0.03	1.61	0.138	2.50
					0.694	1.09	0.36	0.36				0.06	1.88	0.183	1.70
M3H	3.0	He	6.86	1.73	0.365	0.66	0.22	0.22	1250.0[a]	11.9	26.9	0.03	1.75		
					0.670	1.21	0.40	0.40				0.05	2.22		
M1A	1.0	Air	4.76	1.00	0.088	2.68	0.88	0.88	294.0	2.3	55.8	0.005	1.75	0.098	14.87
					0.101	3.10	1.01	1.01				0.005	1.76	0.103	15.33
					0.263	8.04	2.06	2.06				0.015	2.03		
					0.101	3.10	1.01	1.01	920.0[a]	7.3		0.006	1.83		
M1H	1.0	He	4.76	1.00	0.224	6.31	2.06	2.06	1900.0[b]	13.6	55.8	0.015	2.16		

[a]Pebble bed heated air injection. [b]Simulated temperature based on light gas (helium) injection.

Pressure-Sensitive Paint

Innovative Scientific Solutions (ISSI), Inc., brand Uni-FIB pressure-sensitive paint (PSP) was used. The paint contained two parts: an oxygen-permeable fluoroacrylic copolymer binder and a fluorinated platinum porphyrin meso-tetra-pentaflourophenyl porphrine [Pt(TfPP)] oxygen-sensitive probe molecule. The PSP was applied using an airbrush sprayer. The temperature sensitivity was 0.6%/°C. The paint was illuminated with two blue (464 nm) light-emitting diode light sources (0.25 W each). The luminescence output (650 nm) was acquired with a Pixelvision SpectraVideo 16-bit CCD camera (Model SV512V1A/PFT-95). The paint calibration stemmed from the Stern–Volmer relationship, where the pressure was expressed as a function of I_{ref}/I. As suggested by the manufacturer, the calibration data were fit with a second-order polynomial. For the 12-s tunnel run time, five images were taken. ISSI, Inc., PSP_Analysis_2 software was used to average the images. An average background image was then subtracted from both the averaged windoff and averaged windon images. The ratio of the subtracted windoff and the subtracted windon images was then converted into the surface pressure. The PSP_Analysis_2 was also equipped with the calibration file, so that the software directly converted the ratio file into the surface pressure (psiA) using the estimated surface temperature of about 10°C (±5.0°). The overall uncertainty was 3.6% of the measured value.

Flowfield Results

The flow conditions are summarized in Table 1. As indicated, a wide range of injector conditions was examined, and a large volume of data was acquired. In this document, representative data are shown with salient features highlighted. Trends and general conclusions from the entire data set are listed. A more complete database is given by Bowersox and Mahmud.[13]

An important feature noticed from Table 1, which has implications in much of the subsequent discussion, is the effective backpressure ratio,[14] which varied over a range of 0.19–6.15 indicating that underexpanded ($P_{\text{eb}}/P_\infty > 1$), perfectly expanded ($P_{\text{eb}}/P_\infty = 1$), and overexpanded ($P_{\text{eb}}/P_\infty < 1$) injection conditions were present. The majority of the low-blowing-ratio cases studied here were overexpanded.

Flow Visualization

Shadowgraph and schlieren images were acquired for all of the conditions listed in Table 1. These images provided qualitative assessment of the shock structure for the different injectors. The visible features include 1) the missile body shock, 2) the interaction shock, 3) the lambda shock, 4) the recompression shock, and 5) the exit port shock structure—barrel shock for underexpanded injection (faintly visible) and the shock cone for the overexpanded condition. Also noticeable were weak waves (close to the freestream Mach angle) that were generated due to the surface imperfections in the nozzle and test section. Shadowgraph images for models M1A (perfectly expanded), M3A-LP (overexpanded), and M3A-HP (underexpanded) are presented in Figs. 3a, 3b, and 3c, respectively. The freestream flow was from left to right, and the jet flow direction was vertically upward in the positive y direction. The fundamental differences noticed from these images are the jet exit structure, where an oblique shock cone appears in overexpanded injection cases, and a jet barrel shock is faintly visible in the underexpanded cases. To quantify the effect of MPR on the shock structure, the shadowgraphs for different MPR values are superimposed in Figs. 3b and 3c. The higher MPR cases (i.e., high jet pressures) produced stronger and steeper interaction shocks and created the lambda shocks farther upstream. It is observed from the images that the lambda shock size increased with increasing MPR.

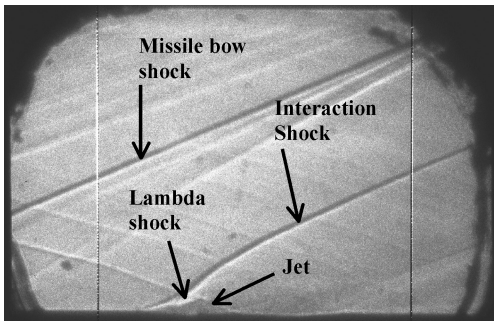

a) M1A, MPR 0.005

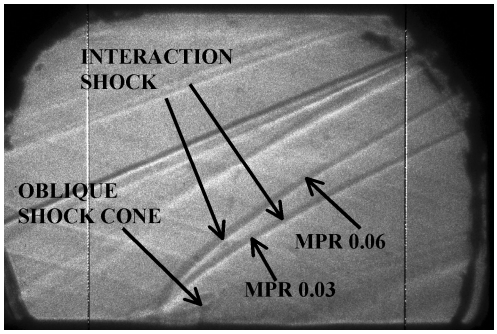

b) M3A-LP (overexpanded jets)

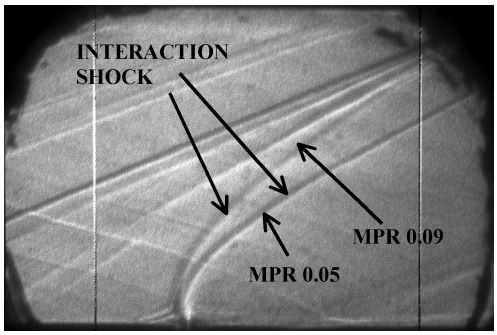

c) M3A-HP (underexpanded jets)

Fig. 3 Representative shadowgraph images (flow from left to right).

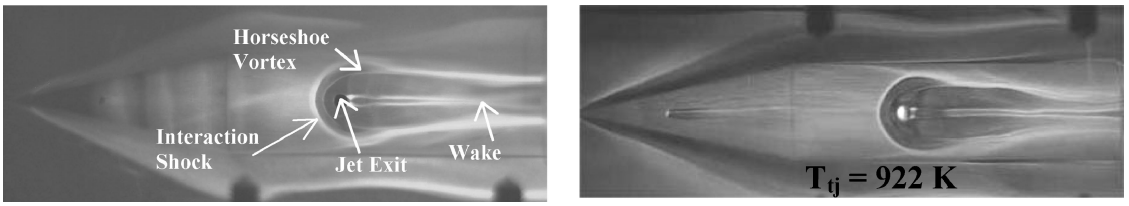

a) High-injection-temperature effects on model M1A, MPR 0.005

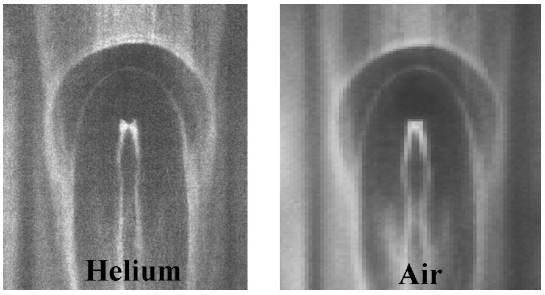

b) High-temperature (1900 K) simulation at MPR 0.015, M_j = 1

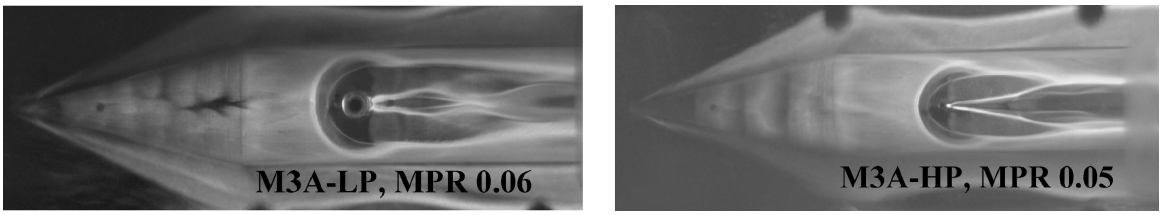

c) Comparison of overexpanded and underexpanded jets

Fig. 4 Representative surface oil flow visualization images.

Surface oil flow visualizations were obtained for all of the conditions listed in Table 1. A representative sample set is shown in Fig. 4. Focusing first on the left-hand image in Fig. 4a, the visible features included 1) the missile body shock at the tip of the missile fuselage, 2) the boundary-layer separation, 3) the jet-interaction region, 4) the interaction shock, 5) the horseshoe vortex, 6) the recompression shock, and 7) the wake region. In Fig. 4, the freestream flow is directed from left to right and the jet flow is directed outward from the paper. Flowfield symmetry is clearly depicted in the images. The missile-body shock angle of 24 deg was estimated from the image, whereas the shock angle calculated from conical theory was 23.8 deg. When the crossflow, downstream of the missile shock, encountered the expansion edge of the missile fuselage, it deflected and marched parallel to the cylindrical missile fuselage. The jet plume acted as an obstacle to the crossflow; this resulted in the boundary-layer separation upstream of the jet and created the interaction shock. The round thick line of oil accumulation represents the separation line due to the interaction shock. The lambda shock in between the boundary-layer separation point and the interaction shock cannot be identified in SOFV images. However, the lambda shocks were clearly visible in shadowgraph images. The next thin oil line that wrapped around the jet was interpreted as the horseshoe vortex.[15] Two other distinct oil lines were observed downstream of the jet. These lines were created due to the wake vortices.[7] The crossflow stream that wrapped around the jet merged to create the compression shocks that appeared downstream of the jet.

A comparison of the SOFVs for models M1A, M3A-LP, and M3A-HP is presented in Figs. 4a–4c. Figure 4a for model M1A compares the temperature effects with high injection temperature (900 K). Champigny and Lacau[1] reported that higher jet temperatures shift the separation line farther upstream; however, in the present study, a 300% increase in the injection static temperature resulted in only a 4.0% increase in the boundary-layer separation distance. The most likely cause for this discrepancy is that the data presented in the literature are for high blowing ratios, which are highly underexpanded. Underexpanded jets create larger upstream flow disturbances than overexpanded jets; thus, the temperature effects are likely to be more significant. To simulate an even higher temperature air injection, the M1A injector was operated with helium at MPR of 0.015 (Fig. 4b). Air was also used at the same MPR (0.015) for comparison purposes. The helium injection was equivalent to the air injection at a temperature of 1900 K. Only slight changes in the flow separation distance were observed. No significant change in the flow structure was observed (discussed next regarding Fig. 5b).

The SOFV for the Mach 3 models are presented in Fig. 4c. Both underexpanded and overexpanded images are shown here. The flow features are analogous to those seen for sonic injection cases except in the wake region. Specifically, the oil lines immediately downstream of the jet moved farther apart while progressing downstream until about $2.5D_e$ for the overexpanded case and about $7D_e$ for the underexpanded case from the injection port. These two lines merged at about $4.5D_e$ downstream in the overexpanded jet and created a diamond-shaped structure.

Figure 5a presents the variation of the separation distance, normalized by injector diameter, with respect to the MPR, for all of the test cases. The uncertainty was estimated at 250 μm. Overall, the expected trend of increasing of the separation distance with increasing MPR was observed. However, MPR alone is not a sufficient correlation parameter, where systematic increases in separation distance with increasing injection pressure and temperature were discerned. For example, separation distances for model M3A-HP were significantly higher than that for model M3A-LP. An explanation for this trend can be found by referring back to Table 1. Specifically, the M3A-HP cases were underexpanded and, hence, the plume expanded on entering crossflow. Thus, the size of the obstruction increased, compared to the M3A-LP case, where the flow was overexpanded.

Figure 5b shows the effect of injection temperature on separation distance. Over the range of conditions tested here, the separation distance for a given MPR increased at a rate of 0.0125 with the jet-to-freestream temperature ratio. It is anticipated that if the high-temperature jets were operated in an overexpanded condition, the influence of temperature would have been more substantial.

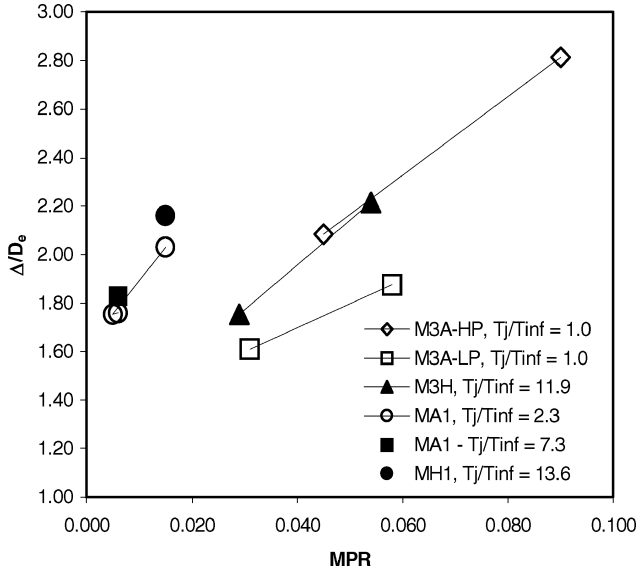

a) MPR

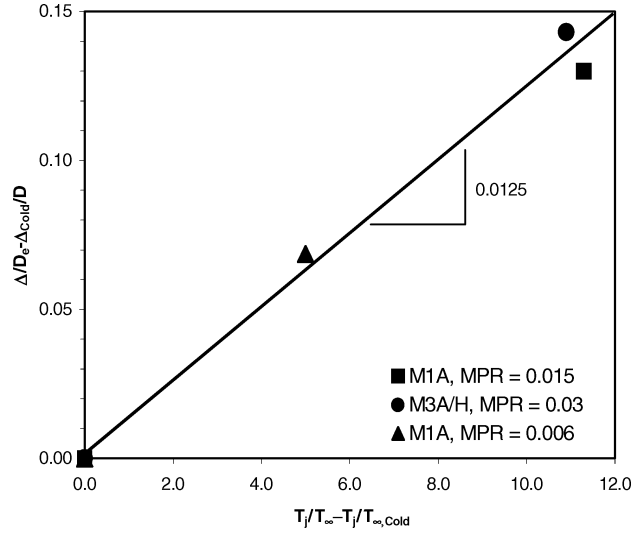

b) Injection temperature

Fig. 5 Boundary-layer separation distance.

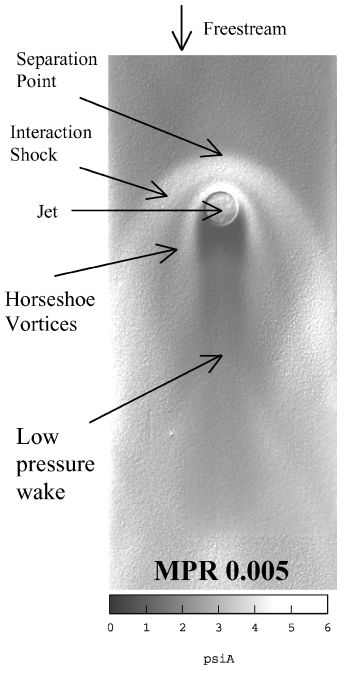

a) Model M1A

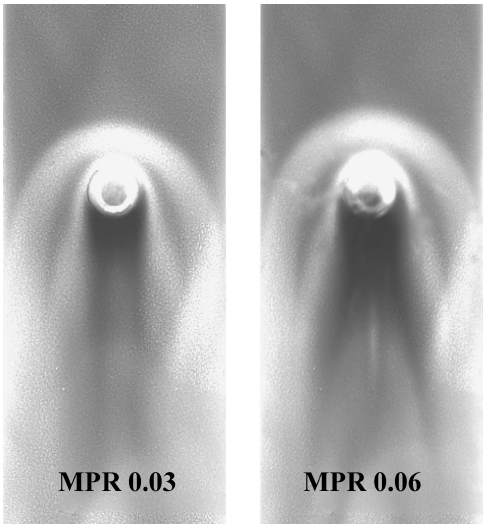

b) Model M3A-LP

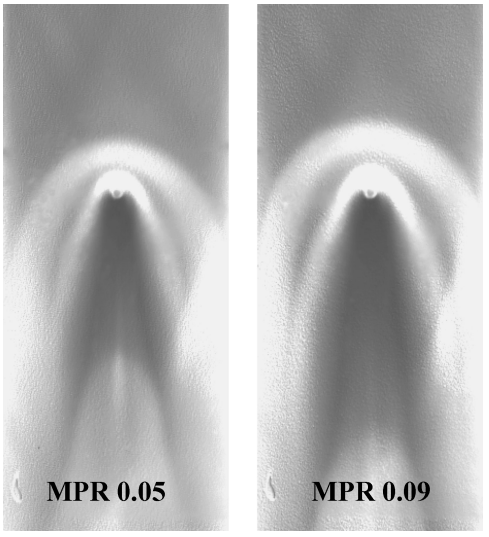

c) Model M3A-HP

Fig. 6 Surface pressure contours.

Pressure-Sensitive Paint

The PSP data were acquired for the same cases discussed earlier. General flowfield features are labeled in Fig. 6a for model M1A. The freestream flows from top to bottom in the images. A common scale with a range from 0 to 6.0 psia was employed so that direct comparisons could be made. The entire painted image area was nominally 36.0 × 83.0 mm. This region covered about 30.0 mm upstream and about 54.0 mm downstream of the injection center. The images were taken through the ceiling of the test section, and so a two-dimensional projection of the curved surface (missile fuselage) was imaged onto the CCD camera. The noticeable flowfield features are boundary-layer separation point, interaction shock, horseshoe vortex, and the low-pressure wake region. Two high-pressure regions upstream of the jet were observed, which is consistent with the work by Gruber et al.[16] The compression due to the interaction shock and the horseshoe vortex created these high-pressure areas. Upstream of the interaction shock, boundary-layer separation occurred and, thus, a recirculation region was created, which can be seen as the first thick semicircular high-pressure region upstream of the jet.

The pressure contours for all the models were qualitatively similar. However, the pressure in the separation region was observed to increase with increasing MPR (injection pressure), and the boundary-layer separation point moved farther upstream with increased MPR. The size of the wake region and the decrease in the

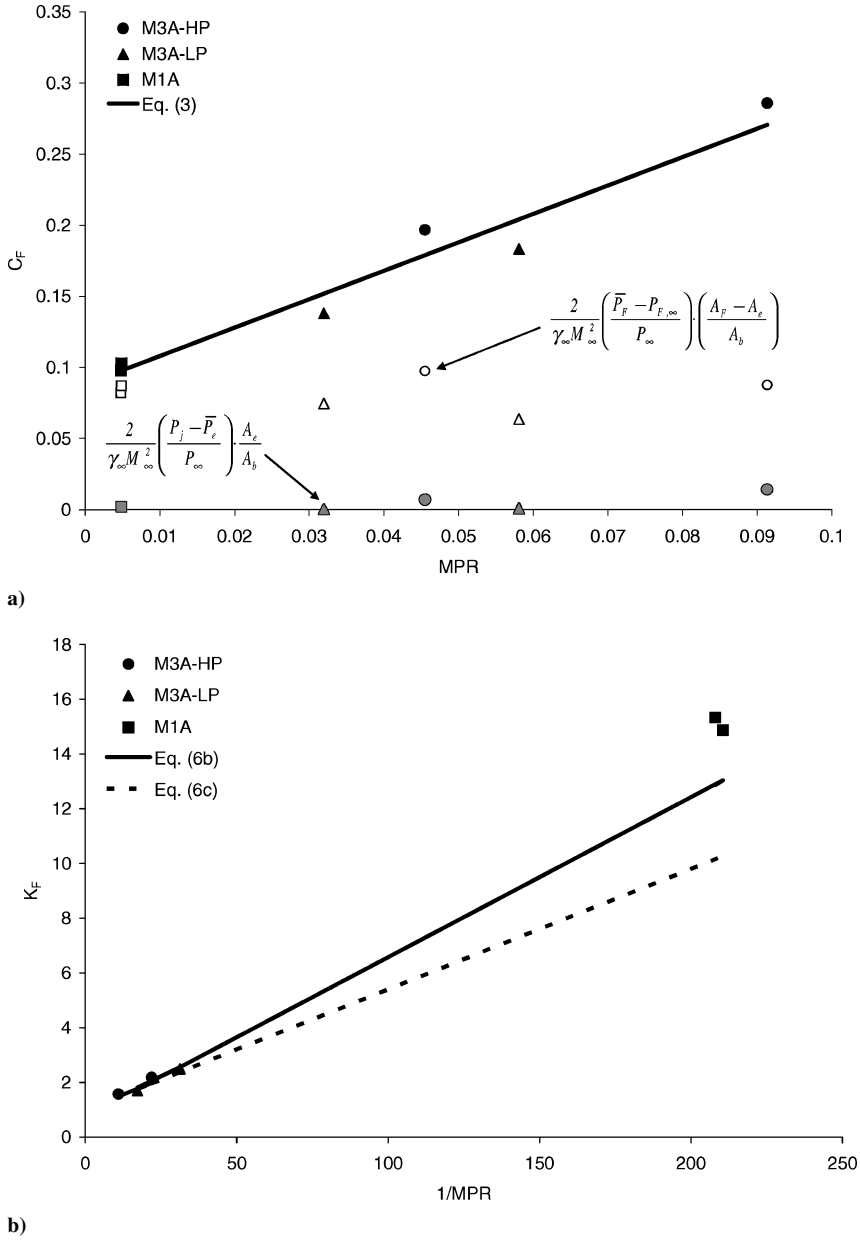

Fig. 7 Effect of MPR on jet control force.

wake pressure both increased with increasing MPR. Previous studies, both experimental and numerical,[1,4,10] demonstrated trends in the centerline longitudinal surface pressure distributions that were similar to those found here.

The net or total force produced by the jet and the associated surface interaction is given by

$$F = \dot{m}_j v_j + (P_j - \bar{P}_e)\cdot A_e + (\bar{P}_F - P_{F,\infty})\cdot(A_F - A_e) \quad (1)$$

The first terms in Eq. (1) make up the familiar rocket thrust equation, and the second term results from the pressure distribution on the fuselage surface. The jet control force coefficient is plotted in Fig. 7a vs the jet MPR (solid black symbols). The data appear to be reasonably linear in this range of MPR, which is consistent with the force coefficient equation derived from Eq. (1); that is,

$$C_F = 2\text{MPR} + \frac{2}{\gamma_\infty M_\infty^2}\left[\left(\frac{P_j - \bar{P}_e}{P_\infty}\right)\cdot\frac{A_e}{A_b} + \left(\frac{\bar{P}_F - P_{F,\infty}}{P_\infty}\right)\cdot\left(\frac{A_F - A_e}{A_b}\right)\right] \quad (2)$$

The two terms that make up the intercept in Eq. (2) are also plotted in Fig. 7a (open symbols and solid gray symbols). These data show that the second term in the bracket in Eq. (2) is much larger than the first. There does appear to be a systematic dependence of the intercept on the injector configuration. However, this dependence is mild, where the average value of the intercept is 0.088 ± 0.015. Thus, for the present range of experiments, Eq. (2) reduced to

$$C_F \simeq 2\text{MPR} + 0.088 \quad (3)$$

Equation (3) is included in Fig. 7a, and the results show that this equation is a reasonable representation of the results. Noteworthy here is the fact that the present experimental configuration prohibited inclusion of potential deamplification due to the shocks wrapping around the lower surface of the fuselage. This deamplification would most likely reduce the intercept of the linear fit.

The jet-interaction performance is generally expressed in terms of the force amplification factor[1] K_F. The amplification factor is defined as the ratio of the total reaction force and the total jet delivered force at the freestream pressure; that is,

$$K_F = F/F_j \quad (4)$$

where $F_j = \dot{m}_j v_j - P_\infty A_e$. Noting that $\dot{m}_j v_j = \gamma_j P_j M_j^2 A_e$, F_j can be rewritten as $\gamma_j P_j M_j^2 A_e(1 - P_\infty/\gamma_j P_j M_j^2)$. With this, Eq. (4) simplifies to

$$K_F = \frac{\gamma_j P_j M_j^2 A_e + (P_j - \bar{P}_e)\cdot A_e + (\bar{P}_F - P_{F,\infty})\cdot(A_F - A_e)}{\gamma_j P_j M_j^2 A_e\left(1 - P_\infty/\gamma_j P_j M_j^2\right)} \tag{5}$$

For high-altitude, high-pressure cases, $P_\infty/\gamma_j P_j M_j^2 \ll 1$. Applying the binomial expansion to the denominator for this case results in the following approximation to Eq. (5):

$$\begin{aligned} K_F \simeq 1 &+ \frac{1}{\gamma_\infty M_\infty^2}\left[\left(1 + \frac{P_j - \bar{P}_e}{P_\infty}\right)\frac{A_e}{A_b} \right. \\ &\left. + \left(\frac{\bar{P}_F - P_{F,\infty}}{P_\infty}\right)\left(\frac{A_F - A_e}{A_b}\right)\right]\frac{1}{\text{MPR}} \\ &+ \frac{1}{\left(\gamma_\infty M_\infty^2\right)^2}\left[\left(\frac{P_j - \bar{P}_e}{P_\infty}\right)\frac{A_e}{A_b} \right. \\ &\left. + \left(\frac{\bar{P}_F - P_{F,\infty}}{P_\infty}\right)\left(\frac{A_F - A_e}{A_b}\right)\right]\frac{A_e}{A_b}\frac{1}{\text{MPR}^2} \end{aligned} \tag{6a}$$

For the Mach 3 injectors, $P_\infty/\gamma_j P_j M_j^2$ was nominally 0.08. Hence, Eq. (6) is applicable. For this case, Eq. (6) is further simplified by noting that for the present Mach 3 injectors the second term in each of the brackets is much larger than the first. Thus, neglecting the first term in each of the brackets and substituting the numerical values from Fig. 7a for the second terms results in

$$\begin{aligned} K_F &\simeq 1 + \frac{1}{\gamma_\infty M_\infty^2}\left[\left(\frac{\bar{P}_F - P_{F,\infty}}{P_\infty}\right)\left(\frac{A_F - A_e}{A_b}\right)\right] \\ &\quad \times \left(1 + \frac{A_e}{A_b}\frac{1}{\gamma_\infty M_\infty^2}\frac{1}{\text{MPR}}\right)\frac{1}{\text{MPR}} \\ &\approx 1 + 0.044\left(1 + \frac{A_e}{A_b}\frac{1}{\gamma_\infty M_\infty^2}\frac{1}{\text{MPR}}\right)\frac{1}{\text{MPR}} \end{aligned} \tag{6b}$$

If the jet area is small compared to the fuselage area, the second term in the bracket in the second line of Eq. (6b) is small compared to unity. Thus, Eq. (6b) can be further simplified to

$$\begin{aligned} K_F &\simeq 1 + \frac{1}{\gamma_\infty M_\infty^2}\left[\left(\frac{\bar{P}_F - P_{F,\infty}}{P_\infty}\right)\left(\frac{A_F - A_e}{A_b}\right)\right]\frac{1}{\text{MPR}} \\ &\approx 1 + \frac{0.044}{\text{MPR}} \end{aligned} \tag{6c}$$

The experimentally measured amplification factors for are shown plotted in Fig. 7b vs 1/MPR. The Mach 3.0 injector data are in good agreement with Eqs. (6a) and (6b). Also included in Fig. 7b are the amplification results for the sonic injector. For the sonic injectors, the MPR was very low, and $P_\infty/\gamma_j P_j M_j^2$ was nominally 0.7–0.75. Hence, the simplifications leading to Eqs. (6a–6c) are not applicable for the M1A model. The sonic data suggest that for the very low MPR cases, the amplification factor is nonlinear in 1/MPR and above the extrapolated trends suggested by Eq. (6).

Conclusions

An experimental analysis of the mean flow properties for sonic and Mach 3 injection into a Mach 3 freestream was accomplished. The range of conditions included MPR = 0.005–0.09, $P_j/P_\infty = 0.6$–19.0, $T_j/T_\infty = 1.0$–13.6 (helium was used to simulate the highest temperature), $\gamma = 1.4$ and 1.67, and $P_{\text{eb}}/P_\infty = 0.19$–$6.15$ (overexpanded, perfectly expanded, and underexpanded jets tested). An extensive characterization of the high-speed jet-interaction flowfield over a blended-body missile fuselage (sharp-coned cylinder) was experimentally achieved, where specific pragmatic and scientific flowfield conclusions were drawn and are summarized in the following.

First, injection temperature for a given MPR had a small but discernible effect on the boundary-layer separation distance, where for a given MPR the separation distance increased with temperature ratio at a rate of approximately 0.013. This increase was smaller than seen in previous overexpanded studies; however, the present high-temperature cases were all overexpanded and, hence, the upstream influence was expected. Second, the boundary-layer separation distance increased significantly with MPR; however, MPR was not a sufficient correlating parameter. For example, for a given MPR, the separation distance increased when the jet condition transitioned from overexpanded to underexpanded. Third, the influence of the jet plume on the surface pressure distribution in the wake region of the flow was found to depend on MPR, where the wake region developed farther downstream in terms of distance nondimensionalized by the jet exit diameter. Fourth, the effective backpressure concept was an accurate indicator of the jet flow condition (overexpanded vs underexpanded), where, for example, a terminating Mach cone was observed for all of the cases that were deemed overexpanded using this criterion. Fifth, the jet interaction bow-shock strength increased with increased MPR. Sixth, for a given MPR, overexpanded jets produced weaker interaction shocks than underexpanded jets, where the overexpanded shock structure turned the flow downstream, thus lessening the flow disturbance. Seventh, the upstream peak pressures associated with lambda shock and the horseshoe vortex increased with increasing MPR. Eighth, the wake pressures decreased with increasing MPR (or injection pressure). Ninth, the interaction force increased almost linearly with increasing MPR. Tenth, the amplification factor varied for the supersonic injectors varied linearly with 1/MPR. However, the very low MPR sonic injectors varied nonlinearly with 1/MPR and the data were above the expected trend.

Acknowledgments

The authors gratefully acknowledge T. Doligalski of the Army Research Office (Grant DAAG55-98-1-0479) for supporting this work.

References

[1]Champigny, P., and Lacau, R. G., "Lateral Jet Control for Tactical Missiles," AGARD Special Course on Missile Aerodynamics, Rept. R-804, June 1994.

[2]Chenault, L., Beran, P., and Bowersox, R., "Second-Order Reynolds Stress Turbulence Modeling of Three-Dimensional Oblique Supersonic Injection," *AIAA Journal,* Vol. 37, No. 10, 1999, pp. 1257–1269.

[3]Kikumoto, K., and Sentoh, E., "Sidejet Aerodynamic Interaction Effects of the Missile," *AIAA Journal*, Vol. 39, No. 4, 2001, pp. 611–617.

[4]Graham, M. J., and Weinacht, P., "Numerical Investigation of Supersonic Jet Interaction for Axisymmetric Bodies," *Journal of Spacecraft and Rockets*, Vol. 37, No. 5, 2000, pp. 675–683.

[5]Srivastava, B., "Lateral Jet Control of a Supersonic Missile: Computational and Experimental Comparisons," *Journal of Spacecraft and Rockets*, Vol. 35, No. 2, 1998, pp. 140–146.

[6]Srivastava, B., "Axisymmetric Divert Jet Performance of a Supersonic Missile: Computational and Experimental Comparisons," *Journal of Spacecraft and Rockets*, Vol. 36, No. 5, 1999, pp. 621–632.

[7]Fric, T. F., and Roshko, A., "Vortical Structure in the Wake of a Transverse Jet," *Journal of Fluid Mechanics*, Vol. 279, Nov. 1994, pp. 1–47.

[8]Kamotani, Y., and Greber, I., "Experiments on a Turbulent Jet in a Crossflow," *AIAA Journal*, Vol. 10, No. 11, 1972, pp. 1425–1429.

[9]Perry, A. E., Kelso, R. M., and Lim, T. T., "Topological Structure of a Jet in a Crossflow," AGARD Meeting on Computational and Experimental Assessment of Jets in Crossflow, AGARD-CP-534, Nov. 1993.

[10]Hsieh, T., "Analysis of the Scaling Effects for Missile Configuration with Lateral Thruster," AIAA Paper 99-0810, Jan. 1999.

[11]Chamberlain, R., McClure, D., and Dang, A., "CFD Analysis of Lateral Jet Interaction Phenomena for the THAAD Interceptor," AIAA Paper 2000-0963, Jan. 2000.

[12]Roger, R. P., "The Aerodynamics of Jet Thrusted Control for Supersonic/Hypersonic Endo-Interceptors: Lessons Learned," AIAA Paper 99-0810, Jan. 1999.

[13]Bowersox, R. D. W., and Mahmud, Z., "Experimental and Numerical Investigation of High-Speed High-Temperature Jet Interaction Flowfields," Texas A&M Univ., Rept. TAMU-HAL-2002-002, Texas A&M Univ., College Station, TX, Nov. 2002.

[14]Schetz, J. A., and Billig, F. S., "Penetration of Gaseous Jets Injected into a Supersonic Stream," *Journal of Spacecraft and Rockets*, Vol. 3, No. 9, 1966, pp. 1658–1665.

[15]Everett, D. E., Woodmansee, M. A., Dutton, J. A., and Morris, M. J., "Wall Pressure Measurement for a Sonic Jet Injected Transversely into a Supersonic Crossflow," *Journal of Propulsion and Power*, Vol. 14, No. 6, 1998, pp. 861–868.

[16]Gruber, M. R., Nejad, A. S., and Goss, L. P., "Surface Pressure Measurements in Supersonic Transverse Injection Flowfields," AIAA Paper 97-3254, July 1997.

W. Williamson
Associate Editor